

Taken as a whole, the data shown in Figs 2 and 3 provide strong evidence that the electrons in metallic carbon nanotubes constitute an LL. Future work will test other predictions of this theory, such as tunnelling between LLs in end-to-end¹ and in crossed geometries²¹. □

Received 2 July; accepted 1 December 1998.

1. Fisher, M. P. A. & Glazman, A. *Mesoscopic Electron Transport* (Kluwer Academic, Boston, 1997).
2. Tarucha, S., Honda, T. & Saku, T. Reduction of quantized conductance at low temperatures observed in 2 to 10 μm -long quantum wires. *Solid State Commun.* **94**, 413–418 (1995).
3. Yacoby, A. *et al.* Nonuniversal conductance quantization in quantum wires. *Phys. Rev. Lett.* **77**, 4612–4615 (1996).
4. Milliken, F. P., Umbach, C. P. & Webb, R. A. Indications of a Luttinger liquid in the fractional quantum Hall regime. *Solid State Commun.* **97**, 309–313 (1996).
5. Chang, A. M., Pfeiffer, L. N. & West, K. W. Observation of chiral Luttinger behavior in electron tunneling into fractional quantum Hall edges. *Phys. Rev. Lett.* **77**, 2538–2541 (1996).
6. Grayson, M. *et al.* Continuum of chiral Luttinger liquids at the fractional quantum Hall edge. *Phys. Rev. Lett.* **80**, 1062–1065 (1998).
7. Wildoer, J. W. G. *et al.* Electronic structure of atomically resolved carbon nanotubes. *Nature* **391**, 59–62 (1998).
8. Odum, T. W., Huang, J., Kim, P. & Lieber, C. M. Atomic structure and electronic properties of single-walled carbon nanotubes. *Nature* **391**, 62–64 (1998).
9. Bockrath, M. *et al.* Single-electron transport in ropes of carbon nanotubes. *Science* **275**, 1922–1925 (1997).
10. Tans, S. J. *et al.* Individual single-wall carbon nanotubes as quantum wires. *Nature* **386**, 474–477 (1997).
11. Egger, R. & Gogolin, A. Effective low-energy theory for correlated carbon nanotubes. *Phys. Rev. Lett.* **79**, 5082–5085 (1997).
12. Kane, C., Balents, L. & Fisher, M. P. A. Coulomb interactions and mesoscopic effects in carbon nanotubes. *Phys. Rev. Lett.* **79**, 5086–5089 (1997).
13. Cobden, D. H. *et al.* Spin splitting and even–odd effects in carbon nanotubes. *Phys. Rev. Lett.* **81**, 681–684 (1998).
14. Tans, S. J., Devoret, M. H., Groeneveld, R. J. A. & Dekker, C. Electron–electron correlations in carbon nanotubes. *Nature* **394**, 761–764 (1998).
15. Grabert, H. & Devoret, M. H. *Single Charge Tunneling: Coulomb Blockade Phenomena in Nanostructures* (Plenum, New York, 1992).
16. Kane, C. L. & Mele, E. J. Size, shape, and low energy electronic structure of carbon nanotubes. *Phys. Rev. Lett.* **78**, 1932–1935 (1997).
17. Bezryadin, A., Verschueren, A. R. M., Tans, S. J. & Dekker, C. Multiprobe transport experiments on individual single-wall carbon nanotubes. *Phys. Rev. Lett.* **80**, 4036–4039 (1998).
18. Matveev, K. A. & Glazman, L. I. Coulomb blockade of tunneling into a quasi-one-dimensional wire. *Phys. Rev. Lett.* **70**, 990–993 (1993).
19. Fisher, M. P. A. & Dorsey, A. Dissipative quantum tunneling in a biased double-well system at finite temperatures. *Phys. Rev. Lett.* **54**, 1609–1612 (1985).
20. Grabert, H. & Weiss, U. Quantum tunneling rates for asymmetric double-well systems with ohmic dissipation. *Phys. Rev. Lett.* **54**, 1605–1608 (1985).
21. Komnik, A. & Egger, R. Nonequilibrium transport for crossed Luttinger liquids. *Phys. Rev. Lett.* **80**, 2881–2884 (1998).

Acknowledgements. We thank S. Louie, M. Cohen, D.-h. Lee, A. Zettl and A. Georges for discussions. This work was supported by DOE (Basic Energy Sciences, Materials Sciences Division, the sp² Materials Initiative). L.B. was supported by the NSF.

Correspondence and requests for materials should be addressed to P.L.M. (mceuen@socrates.berkeley.edu).

The nature of the hydrated excess proton in water

Dominik Marx*, Mark E. Tuckerman†, Jürg Hutter* & Michele Parrinello*

* Max-Planck-Institut für Festkörperforschung, Heisenbergstrasse 1, 70569 Stuttgart, Germany

† Department of Chemistry and Courant Institute of Mathematical Sciences, New York University, 4 Washington Place, New York, New York 10003, USA

Explanations for the anomalously high mobility of protons in liquid water began with Grotthuss's idea^{1,2} of 'structural diffusion' nearly two centuries ago. Subsequent explanations have refined this concept by invoking thermal hopping^{3,4}, proton tunnelling^{5,6} or solvation effects⁷. More recently, two main structural models have emerged for the hydrated proton. Eigen^{8,9} proposed the formation of an H_9O_4^+ complex in which an H_3O^+ core is strongly hydrogen-bonded to three H_2O molecules. Zundel^{10,11}, meanwhile, supported the notion of an H_5O_2^+ complex in which the proton is shared between two H_2O molecules. Here we use *ab initio* path integral^{12–14} simulations to address this question. These simulations include time-independent equilibrium thermal and quantum fluctuations of all nuclei, and determine interatomic

interactions from the electronic structure. We find that the hydrated proton forms a fluxional defect in the hydrogen-bonded network, with both H_9O_4^+ and H_5O_2^+ occurring only in the sense of 'limiting' or 'ideal' structures. The defect can become delocalized over several hydrogen bonds owing to quantum fluctuations. Solvent polarization induces a small barrier to proton transfer, which is washed out by zero-point motion. The proton can consequently be considered part of a 'low-barrier hydrogen bond'^{15,16}, in which tunnelling is negligible and the simplest concepts of transition-state theory do not apply. The rate of proton diffusion is determined by thermally induced hydrogen-bond breaking in the second solvation shell.

Simulating an excess proton in liquid bulk water has proved to be immensely challenging. Based on the efforts of numerous groups, many insights into the microscopic nature of proton hydration and diffusion have been deduced^{17–31,38}. Structural diffusion² as a dynamical process was first 'seen' in microscopic detail in an *ab initio* molecular dynamics study of D^+ in D_2O (ref. 23). It was seen that proton diffusion does not occur via hydrodynamic Stokes diffusion of a rigid complex, but via migration of a structural defect due to a continual interconversion between covalent and hydrogen bonds. Solvent fluctuations modulate the proton transfer barrier and preselect a migration path. The rate-limiting step is the fluctuation-induced breakage of a hydrogen bond between the first and second solvation shell of H_3O^+ , which reduces the coordination number of a water molecule in the first solvation shell²³. It was subsequently suggested that quantum effects could potentially be important for the rattling of the proton in the hydrogen bond²⁴, but it has recently been shown that this depends sensitively on a qualitatively correct model for the interactions²⁷.

The quantum-mechanical particle density 'snapshots' from the present simulations of the hydrated proton give a pictorial realization of the structural diffusion process. Initially, the defect is localized as an H_9O_4^+ structure possessing an H_3O^+ core that donates three hydrogen bonds to neighbouring water molecules (Fig. 1a). In the second frame (Fig. 1b), one of the three protons of the H_3O^+ core migrates along its hydrogen bond and forms an H_5O_2^+ complex, in which this proton becomes equally shared between two water molecules. As the transfer is completed, an H_9O_4^+ complex is formed once again, but now centred on a neighbouring core molecule (Fig. 1c). The onset of further migration is shown in Fig. 1d, where the defect converts into another H_5O_2^+ configuration. Overall (Fig. 1a–d), the structural defect is displaced over a distance corresponding to approximately twice the average water–water distance, that is, about 5 Å. Each individual particle, however, moves by only a fraction of an ångström.

The controversial details of this process can be revealed by examination of the two-dimensional distribution $P(\delta, R_{\text{OO}})$ of the displacement coordinate $\delta = R_{\text{O}_a\text{H}} - R_{\text{O}_b\text{H}}$ of a given proton relative to the instantaneous hydrogen-bond centre and the corresponding bond distance R_{OO} . (See Fig. 1 legend for nomenclature.) For the analysis to be as unbiased as possible, we begin by including all O_aHO_b triples, that is, all hydrogen bonds present in the periodic sample. This distribution (not shown) is characterized by two prominent peaks around $(\delta, R_{\text{OO}}) \approx (\pm 0.9, 2.8)$ Å arising from the hydrogen bonds of bulk water but is manifestly non-zero around $|\delta| \approx 0$ Å. This supports the existence of centrosymmetric complexes, in which the proton is equally shared between two water molecules, and thereby opposes a description solely in terms of H_3O^+ or H_9O_4^+ complexes and/or proton transfer entirely associated with tunnelling.

The analysis can be refined by excluding 'irrelevant' hydrogen bonds in a two-step procedure. First, the H_3O_a^+ defect site is located, and only its three O_aHO_b triples are taken into account. Then, from these three triples, the hydrogen bond with the smallest $|\delta|$ is selected, an intuitive choice based on events of the type in Fig. 1. This second step focuses on the 'most active proton', that is, the one

that has the greatest likelihood of transferring to a neighbouring water molecule, but imposes no *a priori* discrimination between different structures such as H_5O_2^+ or H_9O_4^+ . In the distribution from the first step (not shown), the centrosymmetric $|\delta| \approx 0 \text{ \AA}$ region is substantially enhanced, and two ‘wings’ emerge, which can be attributed to asymmetric hydrogen-bonded defects. After the second step, the distribution (Fig. 2a) acquires a broad and unstructured character. This important finding indicates that the protonic defect can assume many different structures, so that an unambiguous distinction between H_5O_2^+ and H_9O_4^+ can no longer be achieved.

To analyse ‘limiting’ forms of the defect, two windows in the displacement coordinate δ are chosen. Tight δ -margins are deliberately used so that the structural analysis is rendered as evident as possible (see Fig. 2 legend for details). For small $|\delta|$, the structures are found to correspond to an equal sharing of the excess proton between two intact H_2O , in accordance with Zundel’s H_5O_2^+ view of the defect. In contrast, configurations with large $|\delta|$ possess the characteristics of a threefold coordinated H_3O^+ ion, that is, Eigen’s

H_9O_4^+ complex. There are, however, configurations (according to the present δ -margins about half of them) that cannot be characterized as resembling either of these idealized forms.

The fact that a significant portion of the observed structures remain unclassified is also reflected in the shape of $P(\delta, R_{\text{OO}})$ in Fig. 2a. Its structureless ridge allows the defect to evolve easily from H_5O_2^+ to H_9O_4^+ regions, thus implying that the H_5O_2^+ complex cannot be regarded as a typical transition state. Rather, the proton in the most active hydrogen bond oscillates between two water molecules without appreciable hindrance, thereby interconverting two H_3O^+ cores on neighbouring sites via a strongly hydrogen-bonded, centrosymmetric H_5O_2^+ complex. The corresponding effective free-energy barrier (around $\delta = 0 \pm 0.05 \text{ \AA}$ and $R_{\text{OO}} \approx 2.46\text{--}2.48 \text{ \AA}$) is vanishingly small, $\leq 0.15 \text{ kcal mol}^{-1}$, only a fraction of the thermal energy $k_{\text{B}}T \approx 0.59 \text{ kcal mol}^{-1}$ at room temperature. Evidently, both H_5O_2^+ and H_9O_4^+ are only important as limiting structures, and numerous unclassifiable situations exist in between. Therefore, the protonic defect is best visualized as a ‘fluxional complex’.

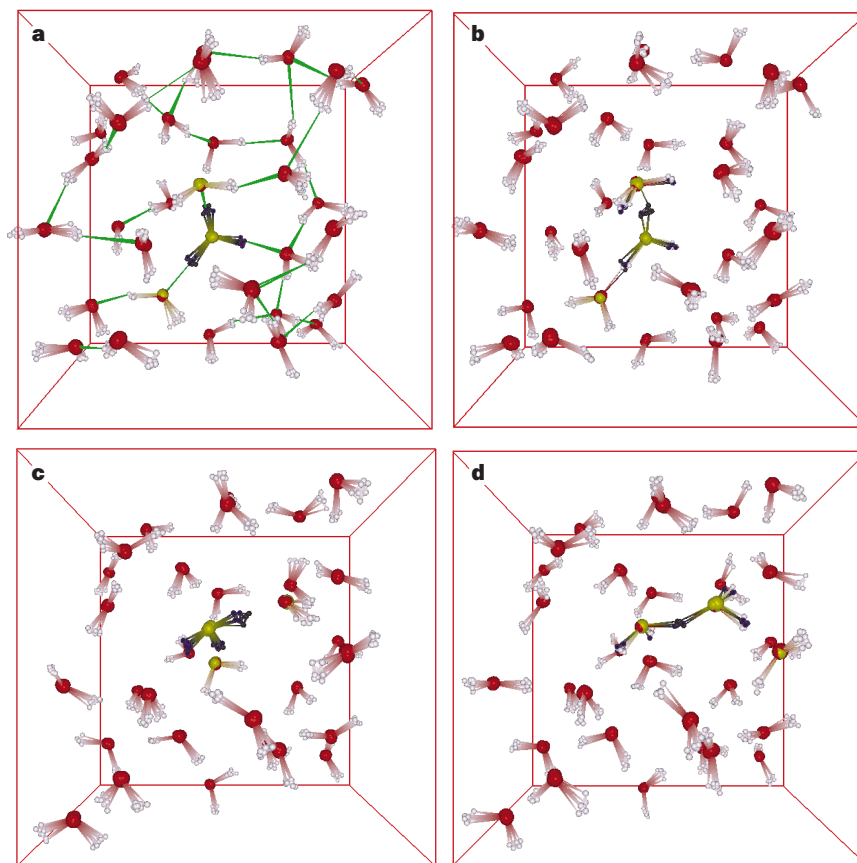


Figure 1 Examples of simulation configurations. We show a perspective view of the particle densities (diagonal part of the nuclear many-body density matrix) of representative single quantum configurations belonging to the proton migration path of the quantum trajectory. We note that the employed *ab initio* path integral molecular dynamics technique^{12–14} does not rigorously produce real-time evolution, but that event sequences can nevertheless be inferred qualitatively. Only the non-periodically replicated atoms (oxygens, red; hydrogens, grey) and bonds are included; hydrogen bonds (green) are sketched only in **a**, the blurring of the atom positions is exclusively due to quantum effects. The defect (given by the H_3O_3^+ core and the triple O_3HO_3 defined in Fig. 2 legend) is indicated separately in every panel by yellow (oxygens) and black (hydrogens). The simulations were performed using CPMD Version 3.0 (J. Hutter, P. Ballone, M. Bernasconi, P. Focher, E. Fois, S. Goedecker, D. Marx, M. Parrinello & M. Tuckerman, Max-Planck-Institut für Festkörperforschung and IBM Zurich Research Laboratory 1995–96) at

ambient conditions using 32 H_2O with one excess proton in a periodic cubic box with a lattice constant of 9.8652 \AA , employing the BLYP density functional^{34,35}, Troullier–Martins pseudo potentials³⁶, and a Γ -point plane wave expansion of the valence orbitals up to 70 rydberg. This particular scheme has been shown to yield a very good description of the water dimer³⁷, the protonated water dimer¹⁶, and bulk water³⁷. The path integral for the quantum simulation^{12–14} was discretized using $P = 8$ Trotter replicas. The normal-mode propagator together with a chain of three coupled Nosé–Hoover thermostats on each degree of freedom was used to generate a canonical distribution at 300 K, improve sampling efficiency, and ensure ergodicity¹⁴. After careful equilibration, quantum and classical trajectories consisting of 100,000 and 160,000 configurations, respectively, were generated (using identical parameters, in particular the same Nosé–Hoover-chain thermostatting scheme).

Having proposed a coherent picture of the structural defect, it remains to identify the rate-determining step. This must be done indirectly, as the path integral approach used provides rigorously only time-averaged quantum equilibrium properties. Comparing the number of distinct net displacements of the defect (such as illustrated in Fig. 1) with the number of (inactive) proton-rattling events, the simulation unambiguously shows that the latter process is not rate-limiting. Rather, a proton localized as H_3O^+ migrates preferentially along the hydrogen bond to the neighbouring H_2O that has the lowest coordination number. A water molecule in the first solvation shell becomes undercoordinated by thermally induced hydrogen-bond breaking between it and a second solvation shell member²³. This phenomenon leads to the coordination number distribution $n(\delta, R_{\text{OO}})$ in the most active hydrogen bond, which is superimposed on $P(\delta, R_{\text{OO}})$ in Fig. 2a. Here, the proton-accepting water molecule is undercoordinated near $|\delta| \approx 0 \text{ \AA}$ (blue to green), where the defect resembles H_5O_2^+ , relative to the wings of the distribution at large $|\delta|$ (red to yellow), where the defect resembles H_9O_4^+ .

How well does a purely classical description of the nuclei, which includes only thermal fluctuations, compare with these quantum results? The answer can be gleaned from Fig. 2b and from the free-energy barrier. In the classical limit, the asymmetric H_9O_4^+ structure

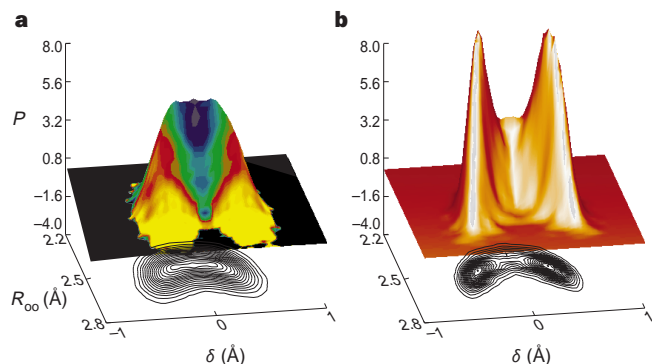


Figure 2 Representation of relative proton positions. Averaged distribution function $P(\delta, R_{\text{OO}})$ of the proton displacement $\delta = R_{\text{O}_a\text{H}} - R_{\text{O}_b\text{H}}$ relative to the O_aHO_b bond midpoint (asymmetric coordinate) and the corresponding oxygen-oxygen separation R_{OO} between the two neighbouring oxygen atoms O_a and O_b from quantum (a) and classical (b) simulations at 300 K. (Definition of the O_aHO_b triple: O_a is the centre of the H_3O^+ unit determined by assigning every proton to its closest oxygen neighbour; H is one of the three protons forming the H_3O^+ unit, such that O_a , H and O_b yield the minimum value of $|\delta|$ in each configuration.) In a, the quantum averaged local coordination number, $n(\delta, R_{\text{OO}})$, of O_b is superimposed on $P(\delta, R_{\text{OO}})$. The function $n(\delta, R_{\text{OO}})$ is obtained by averaging the number of oxygen neighbours of O_b within a sphere of radius R^{cut} for given δ and R_{OO} ; $R^{\text{cut}} = 3.25 \text{ \AA}$ is determined by the first minimum of the oxygen-oxygen radial distribution function $g_{\text{OO}}(r)$ of bulk water. (Colour code: n decreases from yellow (~ 4) to red to green to blue (~ 3.5)). All distributions are smoothed for presentation and symmetrized about $\delta = 0 \text{ \AA}$. In addition, the $P(\delta, R_{\text{OO}})$ distributions are normalized to unity and shown on the same scale. Structural analysis of configurations: (1) for small $|\delta| \leq 0.1 \text{ \AA}$, the first peak of the intra-complex $g_{\text{OO}}(r)$ occurs at $r \approx 2.4 \text{ \AA}$ (compared with 2.8 \AA for bulk water). The first peak of $g_{\text{OH}}(r)$ is around 0.95 \AA (close to the value found in bulk water); a secondary peak occurs close to 1.25 \AA (roughly half of the average OO distance), however, no clearly distinguishable feature exists at $r \approx 1.8 \text{ \AA}$ (where the first intermolecular peak for bulk water would be expected). This pattern for small $|\delta|$ is consistent with an $\text{H}_2\text{O} \cdots \text{H}^+ \cdots \text{OH}_2$ complex, in which a proton is equally shared between two normal water molecules. (2) For large $|\delta| > 0.3 \text{ \AA}$, $g_{\text{OO}}(r)$ peaks near 2.5 \AA , and the first peak of $g_{\text{OH}}(r)$ is, in this case, close to 1.0 \AA (which is slightly longer than for H_2O molecules in the bulk). This corresponds to an $\text{H}_3\text{O}^+ \cdots (\text{H}_2\text{O})_3$ complex, where the H_3O^+ core molecule is roughly threefold coordinated. The first-shell H_2O molecules are themselves approximately fourfold coordinated.

is stabilized owing to an increase in the thermal barrier to $\sim 0.56 \text{ kcal mol}^{-1}$ (approximately $k_B T = 0.59 \text{ kcal mol}^{-1}$). Thus, it is the zero-point energy of the most active proton that shifts the lowest vibrational state towards the top of the classical barrier, thereby enhancing H_5O_2^+ -like complexes, so that the fluctuations of the surrounding water molecules become crucial. This idea is similar to the concept of ‘adiabatic proton transfer’²⁵. Thus, mechanisms such as tunnelling through the classically existing barrier and/or soliton-mediated coherent transfer are of only minor importance. A similar ‘low-barrier hydrogen bond’ situation^{15,16} is also found in the early stage of the pressure-induced transition to symmetric ice X, where proton disorder along the hydrogen bonds is driven by zero-point motion (compare Fig. 2a with Fig. 3c of ref. 32). The essential difference is that in ice X, reduction of the oxygen–oxygen distances (and resulting low barriers) is caused by external pressure, whereas in water it is a consequence of the electrostrictive distortion of the hydrogen-bond network around the structural charge defect. Another indicator of the quantum nature of the structural defect is an increase in the radius of gyration of the H_3O^+ core (see Fig. 3 legend). The difference between the quantum and classical averages, 1.3 \AA versus 0.9 \AA , is due entirely to quantum delocalization of the defect over several hydrogen bonds. The structure of such ‘non-classical’ configurations (see Fig. 3) suggests that these quantum delocalizations, in a sense, ‘probe the most likely direction for further proton migration’, thus enhancing the thermal fluctuations that mainly drive the structural diffusion.

The analysis performed here underlines the complex behaviour of the hydrated proton, bringing out features of both Eigen’s and Zundel’s views, but it also emphasizes that the defect cannot be fully understood using either of these. One tends to think of solution complexes in terms of well-defined structures with transition states in between. We have shown that this appears to be a misleading concept in the context of proton diffusion, and many of the difficulties in the interpretation of the experimental data might

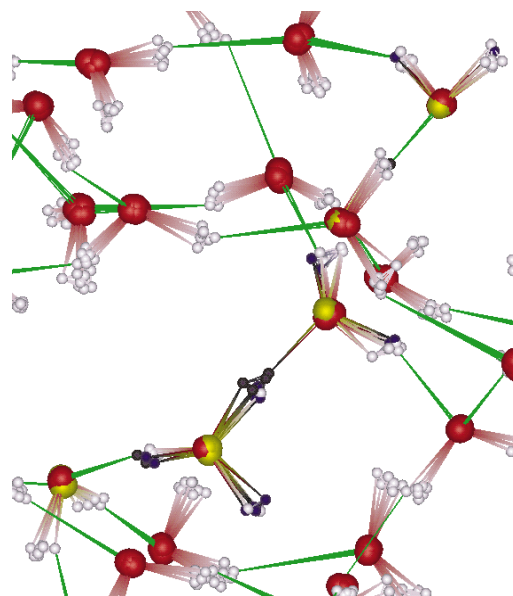


Figure 3 Particle density of a representative delocalized quantum configuration. (See Fig. 1 legend for the definition of the defect and the details of the presentation.) The quantum fluctuations lead to a structural defect that is delocalized over approximately four different hydrogen bonds (lower-left to the upper-right corner). The average ‘size’ of the defects can be quantified by the radius of gyration $R_{\text{H}_3\text{O}^+}^{\text{gr}} = ((1/NP)\sum_s \mathbf{R}_s^i \cdot \mathbf{R}_s^i)^{1/2}$. Here, \mathbf{R}^i is the centroid of the defect given by $\mathbf{R}^i = (1/NP)\sum_s \mathbf{R}_s^i$, i takes values of 1 to N (where $N = 4$, the number of atoms in the H_3O^+ core), $s = 1, \dots, P$ is the Trotter replica index (note that $P = 1$ classically), and angle brackets denote the canonical average.

arise from the attempt to interpret complex behaviour within the limits of a favoured structure. The main conclusions drawn from the present first-principles quantum simulations, together with those of ref. 23, are in accordance with a model that is deduced from, and is claimed to be consistent with, all known experimental data³³. □

Received 12 August; accepted 9 November 1998.

- de Grothuss, C. J. T. Sur la décomposition de l'eau et des corps qu'elle tient en dissolution à l'aide de l'électricité galvanique. *Ann. Chim.* **LVIII**, 54–74 (1806).
- Atkins, P. W. *Physical Chemistry* 6th edn, Ch. 24.8, 741 (Oxford Univ. Press, 1998).
- Hückel, E. Theorie der Beweglichkeiten des Wasserstoff- und Hydroxylions in wässriger Lösung. *Z. Elektrochem.* **34**, 546–562 (1928).
- Stearn, A. E. & Eyring, J. The deduction of reaction mechanisms from the theory of absolute rates. *J. Chem. Phys.* **5**, 113–124 (1937).
- Bernal, J. D. & Fowler, R. H. A theory of water and ionic solution, with particular reference to hydrogen and hydroxyl ions. *J. Chem. Phys.* **1**, 515–548 (1933).
- Wannier, G. Die Beweglichkeit des Wasserstoff- und Hydroxylions in wässriger Lösung. *Ann. Phys. (Leipz.)* **24**, 545–590 (1935).
- Huggins, M. L. Hydrogen bridges in ice and liquid water. *J. Phys. Chem.* **40**, 723–731 (1936).
- Wicke, E., Eigen, M. & Ackermann, Th. Über den Zustand des Protons (Hydroniumions) in wässriger Lösung. *Z. Phys. Chem. (N.F.)* **1**, 340–364 (1954).
- Eigen, M. Proton transfer, acid–base catalysis and enzymatic hydrolysis. *Angew. Chem. Int. Edn Engl.* **3**, 1–19 (1964).
- Zundel, G. & Metzger, H. Energiebänder der tunnelnden Überschuss-Protonen in flüssigen Säuren. Eine IR-spektroskopische Untersuchung der Natur der Gruppierungen $H_3O_2^+$. *Z. Physik. Chem. (N.F.)* **58**, 225–245 (1968).
- Zundel, G. in *The Hydrogen Bond—Recent Developments in Theory and Experiments. II. Structure and Spectroscopy* (eds Schuster, P., Zundel, G. & Sandorfy, C.) 683–766 (North-Holland, Amsterdam, 1976).
- Marx, D. & Parrinello, M. Ab initio path-integral molecular dynamics. *Z. Phys. B (Rapid Note)* **95**, 143–144 (1994).
- Marx, D. & Parrinello, M. Ab initio path integral molecular dynamics: basic ideas. *J. Chem. Phys.* **104**, 4077–4082 (1996).
- Tuckerman, M. E., Marx, D., Klein, M. L. & Parrinello, M. Efficient and general algorithms for path integral Car–Parrinello molecular dynamics. *J. Chem. Phys.* **104**, 5579–5588 (1996).
- Cleland, W. W. & Kreevoy, M. M. Low-barrier hydrogen bonds and enzymic catalysis. *Science* **264**, 1887–1890 (1994).
- Tuckerman, M. E., Marx, D., Klein, M. L. & Parrinello, M. On the quantum nature of the shared proton in hydrogen bonds. *Science* **275**, 817–820 (1997).
- Guisani, Y., Guillot, B. & Bratos, S. The statistical mechanics of the ionic equilibrium of water: a computer simulation study. *J. Chem. Phys.* **88**, 5850–5856 (1988).
- Halley, J. W., Rustad, J. R. & Rahman, A. A polarizable, dissociating molecular dynamics model for liquid water. *J. Chem. Phys.* **98**, 4110–4119 (1993).
- Tuñón, I., Silla, E. & Bertrán, J. Proton solvation in liquid water. An ab initio study using the continuum model. *J. Phys. Chem.* **97**, 5547–5552 (1993).
- Laria, D., Ciccotti, G., Ferrario, M. & Kapral, R. Activation free energy for proton transfer in solution. *Chem. Phys.* **180**, 181–189 (1994).
- Komatsuzaki, T. & Ohmine, I. Energetics of proton transfer in liquid water. I. Ab initio study for origin of many-body interaction and potential energy surfaces. *Chem. Phys.* **180**, 239–269 (1994).
- Wei, D. & Salahub, D. R. Hydrated proton clusters and solvent effects on the proton transfer barrier: a density functional study. *J. Chem. Phys.* **101**, 7633–7643 (1994).
- Tuckerman, M., Laasonen, K., Sprik, M. & Parrinello, M. Ab initio molecular dynamics simulation of the solvation and transport of H_3O^+ and OH^- ions in water. *J. Phys. Chem.* **99**, 5749–5752 (1995); Ab initio molecular dynamics simulation of the solvation and transport of hydronium and hydroxyl ions in water. *J. Chem. Phys.* **103**, 150–161 (1995).
- Lobaugh, J. & Voth, G. A. The quantum dynamics of an excess proton in water. *J. Chem. Phys.* **104**, 2056–2069 (1996).
- Ando, K. & Hynes, J. T. Molecular mechanism of HCl acid ionization in water: ab initio potential energy surfaces and Monte Carlo simulations. *J. Phys. Chem. B* **101**, 10464–10478 (1997).
- Schmidt, R. G. & Brickmann, J. Molecular dynamics simulation of the proton transport in water. *Ber. Bunsenges. Phys. Chem.* **101**, 1816–1827 (1997).
- Sagnella, D. E. & Tuckerman, M. E. An empirical valence bond model for proton transfer in water. *J. Chem. Phys.* **108**, 2073–2083 (1998).
- Vuilleumier, R. & Borgis, D. Quantum dynamics of an excess proton in water using an extended empirical valence-bond hamiltonian. *J. Phys. Chem. B* **102**, 4261–4264 (1998).
- Schmitt, U. W. & Voth, G. A. Multistate empirical valence bond model for proton transport in water. *J. Phys. Chem. B* **102**, 5547–5551 (1998).
- Billeter, S. R. & van Gunsteren, W. F. Protonizable water model for quantum dynamical simulations. *J. Phys. Chem. A* **102**, 4669–4678 (1998).
- Kochanski, E., Kelterbaum, R., Klein, S., Rohmer, M. M. & Rahmouni, A. Decades of theoretical work on protonated hydrates. *Adv. Quantum Chem.* **28**, 273–291 (1997).
- Benoit, M., Marx, D. & Parrinello, M. Tunneling and zero-point motion in high-pressure ice. *Nature* **392**, 258–261 (1998).
- Agmon, N. The Grothuss mechanism. *Chem. Phys. Lett.* **244**, 456–462 (1995); Hydrogen bonds, water rotation and proton mobility. *J. Chim. Phys.-Chim. Biol.* **93**, 1714–1736 (1996).
- Becke, A. D. Density-functional exchange-energy approximation with correct asymptotic behavior. *Phys. Rev. A* **38**, 3098–3100 (1988).
- Lee, C., Wang, W. & Parr, R. G. Development of the Colle–Salvetti correlation-energy formula into a functional of the electron density. *Phys. Rev. B* **37**, 785–789 (1988).
- Troullier, N. & Martins, J. L. Efficient pseudopotentials for plane-wave calculations. *Phys. Rev. B* **43**, 1993–2006 (1991).
- Sprik, M., Hutter, J. & Parrinello, M. Ab initio molecular dynamics simulation of liquid water: comparison of three gradient-corrected density functionals. *J. Chem. Phys.* **105**, 1142–1152 (1996).
- Ojamäe, L., Shavitt, I. & Singer, S. J. Potential models for simulations of the solvated proton in water. *J. Chem. Phys.* **109**, 5547–5564 (1998).

Acknowledgements. We thank K.-D. Kreuer for discussions. The calculations were performed on the Cray-T3E/816 of the Max-Planck-Gesellschaft.

Correspondence and requests for materials should be addressed to D.M. (e-mail: marx@pr.mpi-stuttgart.mpg.de).

Discrete alternating hotspot islands formed by interaction of magma transport and lithospheric flexure

Christoph F. Hieronymus* & David Bercovic†

* Danish Lithosphere Centre, Øster Voldgade 10 L, 1350 Copenhagen K, Denmark

† Department of Geology and Geophysics, University of Hawaii, Honolulu, Hawaii 96822, USA

The large-scale geometry and age progression of many hotspot island chains, such as the Hawaiian–Emperor chain, are well explained by the steady movement of tectonic plates over stationary hotspots. But on a smaller scale, hotspot tracks are composed of discrete volcanic islands whose spacing correlates with lithospheric thickness¹. Moreover, the volcanic shields themselves are often not positioned along single lines, but in more complicated patterns, such as the dual line known as the Kea and Loa trends of the Hawaiian islands^{2,3}. Here we make use of the hypothesis that island spacing is controlled by lithospheric flexure¹ to develop a simple nonlinear model coupling magma flow, which feeds volcanic growth, to the flexure caused by volcanic loads on the underlying plate. For a steady source of melt underneath a moving lithospheric plate, magma is found to reach the surface and build a chain of separate volcanic edifices with realistic spacing. If a volcano is introduced away from the axis of the chain, as might occur following a change in the direction of plate motion, the model perpetuates the asymmetry for long distances and times, thereby producing an alternating series of edifices similar to that observed in the Kea and Loa trends of the Hawaiian island chain.

Various models have been proposed to explain the formation of discrete islands within hotspot tracks. Periodicity in island formation may originate in the mantle by solitary waves^{4,5} on, or shear instabilities^{6,7} of, mantle plumes; these models, however, do not explain the observed correlation¹ between island spacing λ and lithospheric thickness H , that is, $\lambda \propto H^{3/4}$. Alternatively, stresses in the lithosphere may generate joints with regular spacing of the order of the thickness of the lithosphere with volcanic eruptions occurring at their intersections⁸; however, the stresses necessary to cause the observed pattern of volcanoes are not well constrained and may require multiple, somewhat *ad hoc*, origins⁸. Our model instead builds on the idea (motivated by the observed correlation between λ and H) that magma flow occurs at locations where the horizontal flexural stresses due to existing islands are approximately zero¹ (that is, at the transition between the flexural depression and the flexural bulge). The model provides a simplified yet self-consistent dynamical system that generates realistic results by taking into account the effects of flexural stresses and erosion of the dyke walls on fracture formation.

The physical processes involved in our model act on greatly varying length and time scales. Whereas the flexural wavelength is of the order of 100 km (ref. 9), and the flexural amplitude changes over timescales of volcano formation ($\sim 10^6$ years; ref. 10), a typical magma-transporting fracture is only 1–10 m wide and forms over timescales of days (ref. 11). A practical approach to treating this disparity in scales is to define the lithosphere's permeability to magma percolation as a continuous field variable, thus treating the average effects of fractures in a continuum mechanical sense. By analogy with the physics of fracture formation and evolution, the permeability is assumed to depend on stresses^{11,12} and total erosion (for example, melting^{13,14} and thermomechanical erosion¹⁵) of the fracture walls.